A Fast Method to Optimize Efficiency and Stray Magnetic Field for Inductive-Power-Transfer Coils Using Lumped-Loops Model

Ming Lu, *Student Member, IEEE*, and Khai D. T. Ngo, *Fellow, IEEE*

***Abstract*—Both the efficiency and stray magnetic field in inductive power transfer are influenced by the design of transmitter and receiver coils. Their synergetic optimization is realized with Pareto front. The conventional method to derive the front requires thousands of finite-element simulations to sweep the physical parameters of the coils, which is time consuming especially for three-dimensional simulations. This paper demonstrates a fast method to optimize the efficiency and stray magnetic field. The windings are replaced by several lumped loops. As long as the number of turns for each loop is known, the efficiency and magnetic field are calculated using permeance matrices and current-to-field matrices. Therefore, sweeping physical parameters in simulation is replaced by sweeping turns numbers of the lumped loops in calculation. Only tens of simulations are required during the entire procedure, which are used to derive the matrices. The Pareto fronts calculated using the lumped-loops model match well with those derived from simulation using parametric sweep. An optimal design selected along the Pareto front was fabricated and measured to verify the calculation accuracy. The verification shows the same efficiency and less than 12.5% difference of the stray magnetic field, for the results from calculation, simulation, and measurement.**

***Index Terms*—Coil, efficiency, electric vehicles (EVs), inductive power transfer (IPT), magnetic field.**

I. Introduction

PLANAR coils are popularly used in inductive power transfer (IPT) for electric vehicles (EVs) [1]–[4]. Using a variety of compensation topologies in IPT circuits [5]–[8], power is delivered from the transmitter coil to the receiver coil across tens of centimeters according to magnetic resonance and near-field coupling. The advantages of IPT include convenience for drivers, safety for charging in humid environments, and dynamic charging when vehicles are moving [9], [10].

The coil-to-coil efficiency is defined as the ratio of the receiver's output power to the transmitter's input power [11]. Losses of the coils contribute 30% to 50% to the total loss of the IPT circuits [12]–[14], which means the system's efficiency will be poor if the coil-to-coil efficiency is low. In order to increase the coil-to-coil efficiency, the physical parameters of the IPT coils should be optimized, such as the inner radii and outer radii of the windings and the distribution of the turns [15]–[18].

The magnetic field is dominant when compared to electric field in the near-field range where IPT operates [19]. There are significant stray magnetic fields around the coils owning to the large air gap between the transmitter and receiver. International Commission on Non-Ionizing Radiation Protection reports that effects such as stimulation of nervous tissues and induction in the retina of phosphenes are caused by exposure to time-varying magnetic field [20]. One method to attenuate the stray magnetic field is to optimize the physical parameters of the planar coils [21], [22].

Since both the coil-to-coil efficiency and stray magnetic field are influenced by the physical design of the IPT coils, their synergetic optimization is important. The Pareto front is suitable for multiobjective optimization and it has been used a lot in the design of converters [23]. In this paper, the synergetic optimization of the coils is implemented with Pareto front as well. The Pareto front of coil-to-coil efficiency versus stray magnetic field is plotted on a two-dimensional (2D) Cartesian coordinate system. The horizontal axis and vertical axis represent the magnetic field and efficiency, respectively. The optimal design of the coils should be selected from the values along the front.

One straightforward way to derive the Pareto front is to sweep all the physical parameters of the planar coils in finite-element simulation. The results from the parametric sweep are plotted on the Cartesian coordinate system to derive the front. However, this takes thousands of simulations, which is very time consuming, especially for the cases when 3-D simulations are required.

This paper demonstrates a faster method for the optimization. Only tens of simulations are required during the entire procedure. In this method, the windings are replaced by several lumped loops. Only tens of simulations are implemented to derive the permeance matrices and current-to-field matrices of the lumped-loops model. The permeance matrices and current-to-field matrices are used to calculate the inductances and stray magnetic fields, respectively. As long as the number of turns for each loop is known, the efficiency and magnetic field are calculated directly from the matrices. Therefore, sweeping physical parameters in finite-element simulation is replaced by

Manuscript received February 4, 2017; revised April 26, 2017; accepted May 19, 2017. Date of publication May 31, 2017; date of current version January 3, 2018. This work was supported by the High Density Integration Consortium in the Center for Power Electronics Systems, Virginia Tech. Recommended for publication by Associate Editor B. Chen. *(Corresponding author: Ming Lu.)*

The authors are with the Center for Power Electronics Systems, Bradley Department of Electrical and Computer Engineering, Virginia Tech, Blacksburg, VA 24061 USA (e-mail: minglu@vt.edu; kdtn@vt.edu).

Color versions of one or more of the figures in this paper are available online at http://ieeexplore.ieee.org.

Digital Object Identifier 10.1109/TPEL.2017.2710141

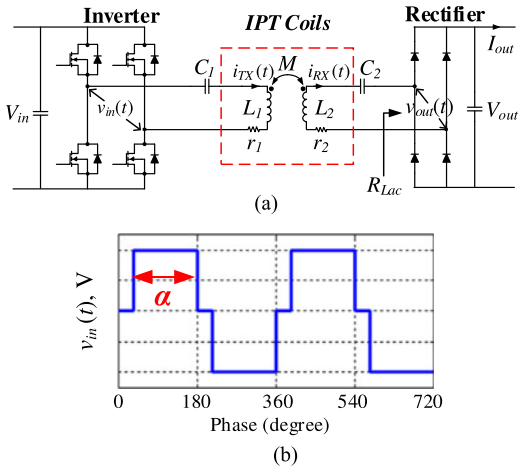

Fig. 1. (a) Circuit topology with series–series compensation for IPT and (b) output voltage of inverter $v_{\rm in}\ (t)$ with phase shift.

sweeping the turns numbers of the lumped loops in calculation. This makes the optimization fast without losing accuracy.

The following section introduces the concepts of coil-to-coil efficiency, stray magnetic field, and the Pareto front for their optimization. Section III demonstrates in detail how to calculate the coil-to-coil efficiency and stray magnetic fields using the lumped-loops model. The Pareto front derived from the lumped-loops model matches well with that derived from parametric sweep in finite-element simulation. In Section IV, a design example of coils, with dimensions of 100 mm × 100 mm and an air gap of 40 mm, was selected along the Pareto front and fabricated for experimental verification. The coil-to-coil efficiencies from calculation and measurement are the same, and the difference for stray magnetic field is less than 12.5%. Section V concludes this paper.

II. Pareto Front of Coil-to-Coil Efficiency Versus Stray Magnetic Field for IPT

A. Coil-to-Coil Efficiency

Different topologies have been proposed to compensate the reactive power in IPT [5]–[8]. Fig. 1(a) shows the circuit topology with series–series compensation. In Fig. 1(a), L_1 and L_2 are the self-inductances of the transmitter and receiver coils; M is the mutual inductance; C_1 and C_2 are the resonant capacitors of L_1 and L_2; r_1 and r_2 are the winding resistances at the switching frequency; $V_{\rm in}$, $V_{\rm out}$, and $I_{\rm out}$ are input voltage, output voltage, and output current. The resonant frequency of C_1 and L_1 is the same as that of C_2 and L_2:

$$1/\sqrt{L_1C_1} = 1/\sqrt{L_2C_2} = 2\pi f_0. \tag{1}$$

Phase-shift regulates the bulk power transferred to the load by controlling the pulse-width α of the inverter's output voltage $v_{\rm in}\ (t)$, as shown in Fig. 1(b).

The simplified circuit model in Fig. 2 is used to analyze the behavior of the circuit in Fig. 1(a). Under the first harmonic approximation, the dc input voltage source $V_{\rm in}$ and the inverter

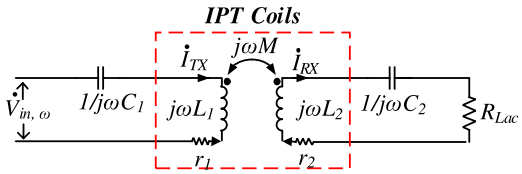

Fig. 2. Simplified circuit model of Fig. 1(a).

are modeled as sinusoidal voltage source $\dot{V}_{{\rm in},\omega}$ in the format of a phasor. The passive rectifier and load are modeled as the equivalent resistor $R_{\rm Lac}$. Phasors $\dot{I}_{TX}$ and $\dot{I}_{RX}$ are the currents of the transmitter and receiver coils, respectively. The values of $\dot{V}_{{\rm in},\omega}$ and $R_{\rm Lac}$ can be expressed as

$$\dot{V}_{{\rm in},\omega} = \left(2\sqrt{2}/\pi\right) V_{\rm in} \sin\left(\alpha/2\right) \angle 0^\circ \tag{2}$$

$$R_{\rm Lac} = \left(8/\pi^2\right) \cdot \left(V_{\rm out}/I_{\rm out}\right). \tag{3}$$

Equations (4) and (5) are derived from the simplified circuit model in Fig. 2

$$\dot{V}_{{\rm in},\omega} = \left[r_1 + j \cdot \left(\omega_s L_1 - 1/\omega_s C_1\right)\right] \dot{I}_{TX} - j \cdot \omega_s M \cdot \dot{I}_{RX} \tag{4}$$

$$0 = j \cdot \omega_s M \cdot \dot{I}_{TX} - \left[r_2 + R_{\rm Lac} + j \cdot \left(\omega_s L_2 - 1/\omega_s C_2\right)\right] \dot{I}_{RX}. \tag{5}$$

The winding resistances r_1 and r_2 include the dc part and ac part. The dc resistance is analytically calculated from the physical parameters of the litz wire, including the cross-sectional area and length. The ac resistance is mostly caused by the proximity effect. Several methods have been proposed to calculate the proximity-effect loss [24]–[27], and this paper applies to the method presented in [25]

$$P_e = \left[\left(\pi l_t N d_c^4\right) / \left(64\rho_c\right)\right] \left\langle \overline{\left(dB(t)/dt\right)^2} \right\rangle \tag{6}$$

where P_e is the proximity-effect loss of a turn; l_t is the average length of the turn; N is the number of strands; d_c is the diameter of the strand; ρ_c is resistivity of copper; $B(t)$ is the time-varying flux density across the turn; $\overline{x}$ is the time average; $\langle x \rangle$ is the spatial average over the turn's cross section. The winding resistances r_1 and r_2 are calculated by adding their corresponding dc and ac resistances.

In order to reduce the circulating energy in the circuit, switching frequency ω_s of the inverter is often set to be the same as the resonant frequency $2\pi f_0$ in (1). Under this condition, the coil-to-coil efficiency, which is defined as the ratio of the receiver's output power to the transmitter's input power, is derived from (4) and (5) as

$$\eta_{\rm coil} = \frac{1}{1 + r_2/R_{\rm Lac} + \left(r_1/R_{\rm Lac}\right) \cdot \left[\left(r_2 + R_{\rm Lac}\right)/\left(\omega_s M\right)\right]^2}. \tag{7}$$

According to (7), the coil-to-coil efficiency is determined by mutual inductance M, winding resistances r_1 and r_2, and the load conditions.

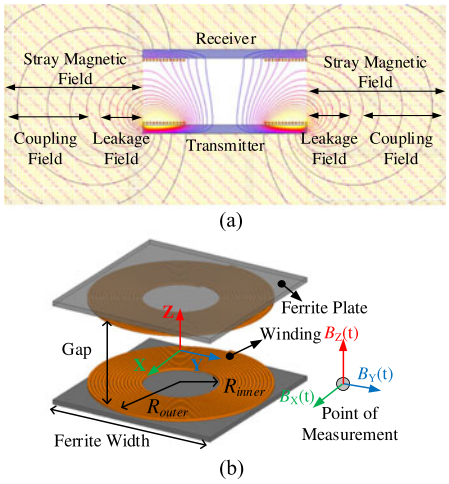

Fig. 3. (a) Flux lines of stray magnetic field around the planar coils for IPT; (b) components of stray magnetic field–$B_X\ (t)$, $B_Y\ (t)$, and $B_Z\ (t)$–in three orthogonal directions.

B. Stray Magnetic Field

Stray magnetic field is defined as the magnetic field around the IPT coils [21], [28], [29]. Its flux lines are shown in Fig. 3(a). The stray magnetic field at one point represents either the leakage field or the coupling field, depending on its distance to the coils.

Stray magnetic field is generated by the winding currents of the transmitter and receiver together. The winding currents, which are sinusoidal, are expressed as

$$i_{TX}(t) = \sqrt{2} I_{TX} \cdot \sin(\omega_s t) \tag{8}$$

$$i_{RX}(t) = \sqrt{2} I_{RX} \cdot \sin(\omega_s t + \theta) \tag{9}$$

where ω_s is the radial frequency of the switching frequency; θ is 90° when the switching frequency equals resonant frequency; I_{TX} and I_{RX} are the rms values of the winding currents which are derived from the simplified circuit model in Fig. 2 as

$$I_{TX} = \left[(r_{RX} + R_{\text{Lac}})/\omega M\right] \left(\pi/2\sqrt{2}\right) I_{\text{out}} \tag{10}$$

$$I_{RX} = \left(\pi/2\sqrt{2}\right) I_{\text{out}}. \tag{11}$$

Fig. 3(b) defines three spatial orientations *X*, *Y*, and *Z*, which are orthogonal to each other. The magnetic field *B* (*t*) at the point of measurement is decomposed into $B_i\ (t)$ $(i = X, Y, Z)$ in these orientations. According to superposition, $B_i\ (t)$ is composed of $B_{TX,i}(t)$ and $B_{RX,i}(t)$, which are generated by the transmitter and receiver currents, respectively. $B_{TX,i}(t)$ and $B_{RX,i}(t)$ are proportional to their corresponding currents as

$$B_{TX,i}(t) = \alpha_{TX,i} \cdot i_{TX}(t) \tag{12}$$

$$B_{RX,i}(t) = \alpha_{RX,i} \cdot i_{RX}(t) \tag{13}$$

where $\alpha_{TX,i}$ and $\alpha_{RX,i}$ are the current-to-field coefficients. The time-varying magnetic fields $B_i\ (t)$ are calculated from

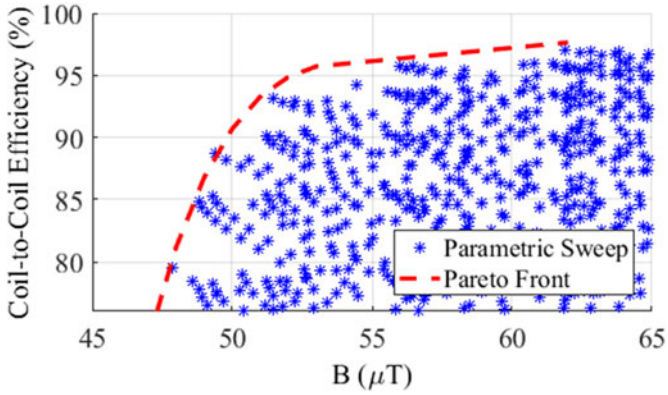

Fig. 4. Pareto front of coil-to-coil efficiency versus stray magnetic field for coils with the structure in Fig. 3(b). The coils are used for the circuit topology in Fig. 1(a) to transfer 100 W of power across a 40 mm gap, with 35 V V_{out} and 100 kHz switching frequency. The maximum dimensions of each coil are limited to 100 mm by 100 mm.

$B_{TX,i}(t)$ and $B_{RX,i}(t)$ as

$$\begin{aligned} B_i(t) &= B_{TX,i}(t) + B_{RX,i}(t) \\ &= \sqrt{2}\left(\alpha_{TX,i} \cdot I_{TX}\right)\sin(\omega_s t) + \sqrt{2}\left(\alpha_{RX,i} \cdot I_{RX}\right) \\ &\quad \times \sin(\omega_s t + \theta). \end{aligned} \tag{14}$$

Equation (14) verifies that $B_i(t)$ is sinusoidal with the switching frequency. The magnetic field $B_i\ (t)$ at the point of measurement is quantified as

$$B = \sqrt{B_X^2 + B_Y^2 + B_Z^2} \tag{15}$$

where B_i is the rms value of the sinusoidal $B_i(t)$. According to (14) and (15), the stray magnetic field is determined by the winding currents and the current-to-field coefficients.

C. Pareto Front of Coil-to-Coil Efficiency Versus Stray Magnetic Field

Since both the coil-to-coil efficiency and stray magnetic field are influenced by the design of the IPT coils, as shown in (7) and (14), their synergetic optimization is important. Pareto front is suitable for this purpose [12], [21], and it is implemented in this paper. The front is plotted on a 2-D Cartesian coordinate system. The horizontal axis and vertical axis represent the magnetic field and coil-to-coil efficiency, respectively. The optimal designs of the coils are selected from the front.

Fig. 4 shows an example of the Pareto front to optimize the coils for the circuit topology in Fig. 1(a). The structure of the coils is the same as Fig. 3(b). The maximum dimensions of each coil are 100 mm by 100 mm. The objective of this design is to transfer 100 W of power across a 40 mm gap, with 35 V output voltage and 100 kHz switching frequency.

Each marker in Fig. 4 represents the coil-to-coil efficiency and stray magnetic field for one set of physical parameters of the coils, including inner radii and outer radii of the winding, distribution of turns, and type of litz wire. The Pareto front is then plotted on the upper left of all the markers. The detailed procedure to derive the Pareto front is introduced in Section III.

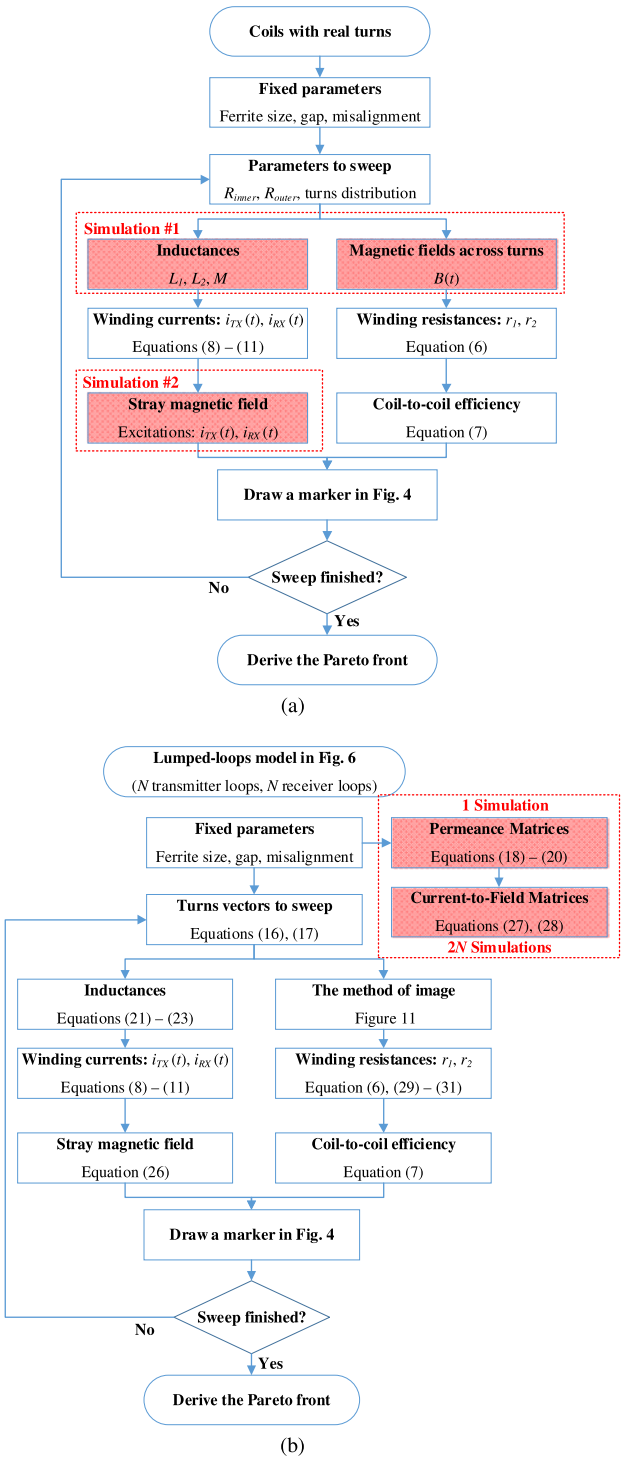

Fig. 5. Procedures to derive the Pareto front of coil-to-coil efficiency versus stray magnetic field with (a) parametric sweep in finite-element simulation and (b) calculation using lumped-loops model.

III. Derive Pareto Front Using Lumped-Loops Model

Fig. 5(a) summarizes the conventional procedure to derive the Pareto front using the parametric sweep in finite-element simulation. In this paper, all the simulations are implemented with Ansys Maxwell [30]. The procedure starts off by drawing the model with real turns in simulation. Physical parameters, including inner radii and outer radii of the windings, as well as the distribution of the turns, are swept. Two simulations are required to obtain the efficiency and magnetic field for each set of physical parameters. In the first simulation, self-inductance of the transmitter L_1, self-inductance of the receiver L_2, mutual inductance M, and the magnetic fields $B(t)$ across the turns are simulated. Then winding resistances r_1 and r_2, winding currents $i_{TX}(t)$ and $i_{RX}(t)$, and coil-to-coil efficiency are calculated from (6), (8) – (11), and (7), respectively. The second simulation excites the windings with $i_{TX}(t)$ and $i_{RX}(t)$ to obtain the stray magnetic field. The coil-to-coil efficiency and stray magnetic field for each set of physical parameters are marked on the Cartesian coordinate system in Fig. 4. The Pareto front is derived from these markers afterward.

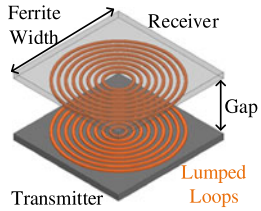

Fig. 6. Lumped-loops model used to start the fast optimization in Fig. 5(b).

However, the method in Fig. 5(a) requires thousands of simulations which are very time consuming. Since the finite-element simulations are inside the iteration of the parametric sweep, $2M$ simulations are required if M kinds of parameters are swept to derive the Pareto front. In order to make the optimization faster, the simulations should be taken out of the iteration. This is realized with the lumped-loops model using the procedure in Fig. 5(b) [29].

In Fig. 5(b), there is no simulation inside the iteration. Only tens of simulations are used to derive the permeance matrices and current-to-field matrices. Generally speaking, there are five major steps in this procedure: determine the lumped-loops model, derive the permeance matrices and current-to-field matrices from simulations, calculate the stray magnetic field, calculate the coil-to-coil efficiency, and plot the Pareto front. The details about each step are provided below.

A. Lumped-Loops Model and Turns Vectors

The procedure in Fig. 5(b) starts off with replacing the original coils with the lumped-loops model. Fig. 6 shows the structure of the lumped-loops model. Several loops are distributed on top of the ferrite plate with equal spacing. Each loop is composed of a certain number of turns.

Turns vectors $\vec{N}_{TX}$ and $\vec{N}_{RX}$ are used to describe the number of turns for each loop

$$\vec{N}_{TX} = \begin{bmatrix} N_{TX1} & N_{TX2} & \cdots & N_{TXN} \end{bmatrix} \tag{16}$$

$$\vec{N}_{RX} = \begin{bmatrix} N_{RX1} & N_{RX2} & \cdots & N_{RXN} \end{bmatrix} \tag{17}$$

where $N_{TX(n)}$ and $N_{RX(n)}$ represent the turns number of the loop in the transmitter and receiver, respectively, with $n = 1, 2, \ldots N$. Loop 1 represents the outermost loop in Fig. 6, while loop N represents the innermost loop.

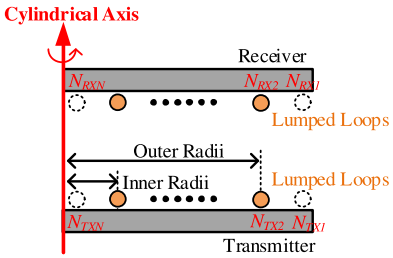

Fig. 7. Cylindrical view of the lumped loops model in Fig. 6. The turns vectors of the transmitter and receiver are $[N_{TX1}, N_{TX2}, \ldots, N_{TXN}]$ and $[N_{RX1}, N_{RX2}, \ldots, N_{RXN}]$, respectively. Physical parameters such as inner radii, outer radii, and distribution of turns are represented by turns vectors.

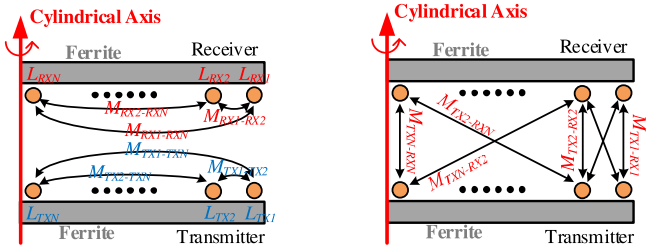

Fig. 8. (a) Elements of permeance matrices in (18) and (19); (b) elements of permeance matrices in (20). All the elements are derived from one finite-element simulation with one turn in each loop.

The physical parameters of coils such as inner radii, outer radii, and distribution of turns are equivalent to the turns vectors. In Fig. 7, loops with dashed circles are assigned zero turns to realize the labeled inner radii and outer radii of the winding. The numbers of turns for the loops with solid circles represent the distribution of turns in the original coils. Therefore, by using the lumped-loops model and turns vectors, the sweep of the physical parameters such as inner radii, outer radii, and distribution of turns is equivalent to the sweep of the elements of the turns vectors in (16) and (17).

The purpose of using a 2-D axial symmetrical structure in Fig. 7 is to better explain the lumped-loops model and to label the elements of turns vector. The concept of the lumped-loops model and the optimization methodology are good for planar winding with other ferrite shapes (e.g., square or rectangular). For example, the lumped-loops model in Fig. 6 is used to optimize the coils structure with square ferrite plate in Fig. 3(b). The windings are replaced by the lumped loops, whereas the ferrite plate is not changed. Three-dimensional finite-element simulations in Ansys Maxwell are implemented to derive the permeance matrices and current-to-field matrices for the lumped loops model in Fig. 6, which will be demonstrated in the following part.

B. Permeance Matrices and Current-to-Field Matrices

Fig. 5(b) shows that $2N + 1$ simulations are required to derive the permeance matrices and current-to-field matrices for a lumped-loops model with N loops in each coil. The permeance matrices and current-to-field matrices are used to calculate the inductances and stray magnetic fields from the turns vectors.

The definition of the permenace matrices is explained with the lumped-loops model in Fig. 8. In this lumped-loops model, each loop has one turn. The permeance matrices $\mathbf{L_{TX}}$ for self-inductance of the transmitter, $\mathbf{L_{RX}}$ for self-inductance of the receiver, and $\mathbf{M}$ for the mutual inductance between the transmitter and receiver are defined as

$$\mathbf{L_{TX}} = \begin{bmatrix} L_{TX1} & M_{TX1-TX2} & \cdots & M_{TX1-TXN} \\ M_{TX2-TX1} & L_{TX2} & \cdots & M_{TX2-TXN} \\ \vdots & \vdots & \ddots & \vdots \\ M_{TXN-TX1} & M_{TXN-TX2} & \cdots & L_{TXN} \end{bmatrix} \tag{18}$$

$$\mathbf{L_{RX}} = \begin{bmatrix} L_{RX1} & M_{RX1-RX2} & \cdots & M_{RX1-RXN} \\ M_{RX2-RX1} & L_{RX2} & \cdots & M_{RX2-RXN} \\ \vdots & \vdots & \ddots & \vdots \\ M_{RXN-RX1} & M_{RXN-RX2} & \cdots & L_{RXN} \end{bmatrix} \tag{19}$$

$$\mathbf{M} = \begin{bmatrix} M_{TX1-RX1} & M_{TX1-RX2} & \cdots & M_{TX1-RXN} \\ M_{TX2-RX1} & M_{TX2-RX2} & \cdots & M_{TX2-RXN} \\ \vdots & \vdots & \ddots & \vdots \\ M_{TXN-RX1} & M_{TXN-RX2} & \cdots & M_{TXN-RXN} \end{bmatrix} \tag{20}$$

where L_{TXn} is the self-inductance of corresponding loop n in the transmitter; $M_{TXn-TXm}$ is the mutual inductance between loops n and m in the transmitter; L_{RXn} is the self-inductance of corresponding loop n in the receiver; $M_{RXn-RXm}$ is the mutual inductance between loops n and m in the receiver; $M_{TXn-RXm}$ is the mutual inductance between loop n in the transmitter and loop m in the receiver.

All the elements of the permeance matrices in (18)–(20) are derived from one finite-element simulation, using the lumped-loops model with one turn for each loop. For example, in order to derive the permeance matrices of the lumped-loops model in Fig. 6, all the loops are excited with 1 A turn, and the permeance matrices are directly extracted from the 3-D simulation using Ansys Maxwell. The gap and ferrite size are fixed according to the specifications of the application.

Inductances L_1, L_2, and M of the coils are calculated with turns vectors $\vec{N}_{TX}$ and $\vec{N}_{RX}$ and permeance matrices $\mathbf{L_{TX}}$, $\mathbf{L_{RX}}$, and $\mathbf{M}$ as

$$L_1 = \vec{N}_{TX}\mathbf{L_{TX}}\vec{N}_{TX}^{T} \tag{21}$$

$$L_2 = \vec{N}_{RX}\mathbf{L_{RX}}\vec{N}_{RX}^{T} \tag{22}$$

$$M = \vec{N}_{TX}\mathbf{M}\vec{N}_{RX}^{T}. \tag{23}$$

The current-to-field matrices are used to calculate the stray magnetic field from the winding currents and turns vectors, as shown in Fig. 9. A similar concept is described in [31]. Since

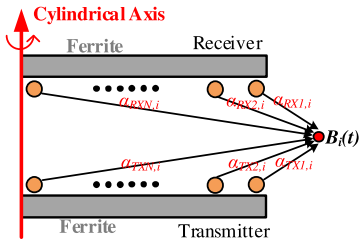

Fig. 9. Elements of current-to-field matrices in (27) and (28) for the lumped-loops model. They are derived from 2*N* simulations. Index *i* represents orientations X, Y, and Z in Fig. 3(b).

the magnetic field is proportional to the winding current, the magnetic field $B_{TXn,i}(t)$ generated by loop *n* of the transmitter coil is calculated as

$$B_{TXn,i}(t) = \alpha_{TXn,i} N_{TXn} i_{TX}(t) \tag{24}$$

where $\alpha_{TXn,i}$ is the current-to-field coefficient for loop *n* of the transmitter; N_{TXn} is the number of turns for this loop; $i_{TX}(t)$ is the winding current of the transmitter; *i* represents the orientations X, Y, or Z in Fig. 3(b).

Similarly, the magnetic field $B_{RXn,i}(t)$ generated by loop *n* of the receiver coil is calculated as

$$B_{RXn,i}(t) = \alpha_{RXn,i} N_{RXn} i_{RX}(t). \tag{25}$$

According to superposition, $B_i(t)$ at the point of measurement in Fig. 9 equals the summation of the magnetic fields generated by all the loops in transmitter and receiver

$$\begin{aligned} B_i(t) &= \sum_{n=1}^{N} \alpha_{TXn,i} N_{TXn} i_{TX}(t) + \sum_{n=1}^{N} \alpha_{RXn,i} N_{RXn} i_{RX}(t) \\ &= \vec{\alpha}_{\mathbf{TX,i}} \vec{N}_{TX}^{\ T} i_{TX}(t) + \vec{\alpha}_{\mathbf{RX,i}} \vec{N}_{RX}^{\ T} i_{RX}(t) \end{aligned} \tag{26}$$

where $\vec{\alpha}_{\mathbf{TX,i}}$ and $\vec{\alpha}_{\mathbf{RX,i}}$ are the current-to-field matrices in the X, Y, and Z orientations for the transmitter and receiver, respectively. They are composed of the current-to-field coefficients in (24) and (25)

$$\vec{\alpha}_{\mathbf{TX,i}} = \begin{bmatrix} \alpha_{TX1,i} & \alpha_{TX2,i} & \cdots & \alpha_{TXN,i} \end{bmatrix} \tag{27}$$

$$\vec{\alpha}_{\mathbf{RX,i}} = \begin{bmatrix} \alpha_{RX1,i} & \alpha_{RX2,i} & \cdots & \alpha_{RXN,i} \end{bmatrix}. \tag{28}$$

The current-to-field coefficients of one loop in Fig. 6 is derived by setting 1 A-turn in this loop and setting 0 A-turns to all the others. For example, when deriving coefficients $\alpha_{TX1,X}$, $\alpha_{TX1,Y}$, and $\alpha_{TX1,Z}$, only the transmitter loop 1 is excited with 1 A-turn in Ansys Maxwell. The simulated magnetic fields B_X, B_Y, and B_Z at the measurement point quantitatively equal the current-to-field coefficients $\alpha_{TX1,X}$, $\alpha_{TX1,Y}$, and $\alpha_{TX1,Z}$, respectively. If there are *N* loops for the transmitter and *N* loops for receiver, 2*N* simulations are required to derive all the elements in the current-to-field matrices.

C. Calculation of Stray Magnetic Field

For each set of turns vectors, the self-inductances L_1, L_2 and mutual inductance *M* of the lumped-loops model are calculated from (21)–(23) using permeance matrices. Winding currents

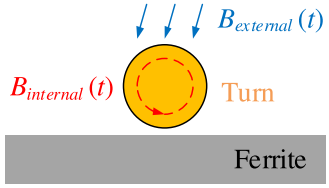

Fig. 10. Internal field B_{internal} and external field B_{external} across one turn of the planar coil.

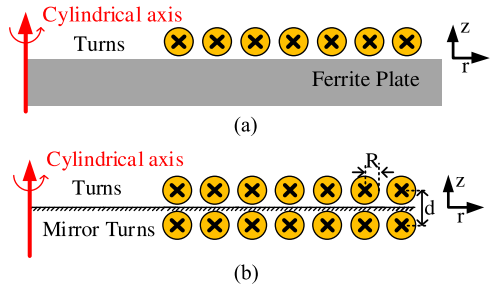

Fig. 11. (a) Planar coils with ferrite plate; (b) equivalent structure using the method of image by replacing ferrite plate with mirrored turns.

$i_{TX}(t)$ and $i_{RX}(t)$ are derived from (8)–(11) with the inductances. The stray magnetic fields in X, Y, and Z orientations are calculated from (26) with winding currents, turns vectors, and current-to-field matrices.

D. Calculation of Coil-to-Coil Efficiency

Winding resistances r_1 and r_2 should be derived for the coil-to-coil efficiency. The magnetic field across each turn is needed to calculate the proximity-effect resistance in (6). To analytically calculate these fields, the lumped-loops model is translated back to the original coils with real turns, according to its turns vectors.

The magnetic field across each turn is composed of internal field $B_{\text{internal}}(t)$ and external field $B_{\text{external}}(t)$, as shown in Fig. 10. The internal field is generated by the turn itself. It is determined by the current distribution of the turn. The external field is generated by all the other turns. When the winding currents are sinusoidal, $\langle \overline{(dB(t)/dt)^2} \rangle$ in (6) is calculated from the internal and external magnetic fields as

$$\left\langle \overline{(dB(t)/dt)^2} \right\rangle = (\omega^2/2)\left(\left\langle B_{\text{internal}}^2 \right\rangle + \left\langle B_{\text{external}}^2 \right\rangle\right) \tag{29}$$

where B_{internal} and B_{external} are the peak magnitudes of the sinusoidal $B_{\text{internal}}(t)$ and $B_{\text{external}}(t)$, respectively; ω is the radial frequency of winding currents.

The existence of the ferrite plate in Fig. 11(a) complicates the calculation of the magnetic fields. According to the method of image [32]–[35], the original planar coil with ferrite plate is replaced by the equivalent structure with mirrored turns in Fig. 11(b). The original turns and mirrored turns are symmetrical about the upper surface of the ferrite plate, and their dimensions and excitations are the same.

The magnetic field $\langle B_{\text{internal}}^2 \rangle$ of one turn is composed of the magnetic field $B_{\text{self}}(t)$, which is generated by the turn itself and the magnetic field $B_{\text{mirror}}(t)$ which is generated by its

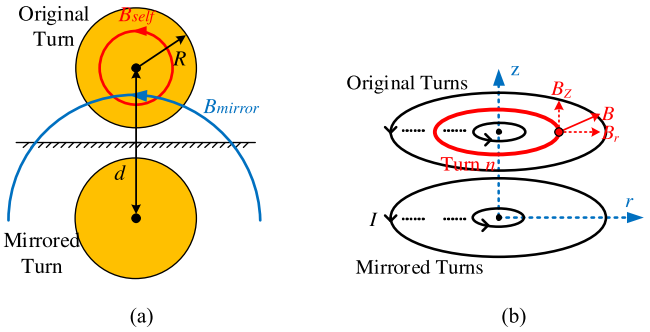

Fig. 12. (a) Cross section of one turn and its mirrored turn to calculate $\langle B^2_{\text{internal}}\rangle$; (b) model to calculate $\langle B^2_{\text{external}}\rangle$ of turn n, which is generated by all the other original turns and their mirrored turns.

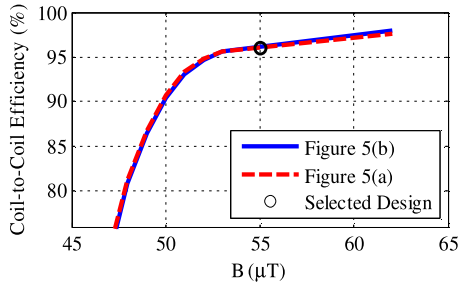

Fig. 13. Comparison of the Pareto fronts derived from the procedures of Fig. 5(a) and (b). The coils were designed to transfer 100 W power across a 40 mm gap using the circuit topology in Fig. 1(a), with 35 V V_{out} and 100 kHz switching frequency. The maximum dimensions of each coil are limited to 100 mm by 100 mm.

mirrored turn, as shown in Fig. 12(a). According to Ampere's Law, $B_{\text{self}}(t)$ and $B_{\text{mirror}}(t)$ are calculated as

$$\begin{aligned}\left\langle B^2_{\text{internal}}\right\rangle &= \left\langle B^2_{\text{self}}\right\rangle + \left\langle B^2_{\text{mirror}}\right\rangle \\ &= \frac{\int_0^R \left(\frac{\mu_0 I}{2\pi r}\cdot\frac{r^2}{R^2}\right)^2 (2\pi r\cdot dr)}{\pi R^2} \\ &\quad + \frac{\int_{-R}^R \left[\frac{\mu_0 I}{2\pi(d+x)}\right]^2 \left(2\sqrt{R^2-x^2}\cdot dx\right)}{\pi R^2} \end{aligned} \tag{30}$$

where R is the radius of the cross section of the turn; d is the distance between the centers of the original turn and the mirrored turn; I is the peak value of the current excitations; and μ_0 is the permeability of free space.

The Biot–Savart Law [36] in the Appendix is used to calculate $\langle B^2_{\text{external}}\rangle$ for one turn, which is generated by all the other turns and their corresponding mirrored turns. In Fig. 12(b), the magnetic field B on a circular turn n is decomposed into B_z in the axial direction and B_r in the radial direction. According to superposition, $\langle B^2_{\text{external}}\rangle$is calculated as

$$\begin{aligned}\left\langle B^2_{\text{external}}\right\rangle &= \left(\sum_{\substack{m=1\\m\neq n}}^{N} B_{r,m-\text{original}} + \sum_{\substack{m=1\\m\neq n}}^{N} B_{r,m-\text{mirror}}\right)^2 \\ &\quad + \left(\sum_{\substack{m=1\\m\neq n}}^{N} B_{z,m-\text{original}} + \sum_{\substack{m=1\\m\neq n}}^{N} B_{z,m-\text{mirror}}\right)^2 \end{aligned} \tag{31}$$

where the magnetic fields generated by the original turn m and the mirrored turn m are represented as $B_{m-\text{original}}$ and $B_{m-\text{mirror}}$, respectively. $B_{m-\text{original}}$ and $B_{m-\text{mirror}}$ are decomposed into components in the radial direction, $B_{r,\,m-\text{original}}$ and $B_{r,\,m-\text{mirror}}$, and components in the axial direction, $B_{z,\,m-\text{original}}$ and $B_{z,\,m-\text{mirror}}$.

The proximity-effect resistance is calculated with $\langle (dB(t)/dt)^2\rangle$, which is derived from (30) and (31). The winding resistances r_1 and r_2 are calculated by adding the dc resistance and proximity-effect resistances. The coil-to-coil efficiency is calculated from (7) with the inductances and winding resistances.

E. Plot the Pareto Front

The coil-to-coil efficiencies and stray magnetic fields calculated for all the turns vectors are marked on the 2-D Cartesian coordinate system. Next, the Pareto front is derived from all these markers. Fig. 13 provides a comparison of the Pareto fronts derived following the procedure in Fig. 5(a) using the parametric sweep in simulation, and Fig. 5(b) by calculation using the fast method and lumped-loops model. The Pareto fronts in Fig. 13 are derived for the coils structure in Fig. 3(b). The coils were designed to transfer 100 W power across a 40 mm gap using the circuit topology in Fig. 1(a), with 35 V V_{out} and 100 kHz switching frequency. The maximum dimensions of each coil are limited to 100 mm by 100 mm. The Pareto fronts in Fig. 13 are almost the same even though they are derived using different methods.

The computational advantages of fast optimization will be quantitatively analyzed, using the Pareto fronts in Fig. 13 as an example. The conventional method derives the Pareto front following the procedure in Fig. 5(a). The physical parameters are swept in finite-element simulation, including the inner radii of winding R_{inner}, outer radii of winding R_{outer}, and turns number. For the specifications in Fig. 13, the inner radii R_{inner} was swept from 5 mm to 45 mm, with 5 mm step. The outer radii R_{outer} was swept from 10 mm to 50 mm, with 5 mm step, and R_{outer} should be larger than R_{inner} during the sweep. Turns number are swept from 5 turns to 50 turns. A total number of 2070 simulations are required to derive the Pareto front using the conventional method. Assuming each simulation requires 2 min, a total of 69 h are required to finish all the simulations. In some applications, the turns of winding are not evenly distributed, and that will require even more simulations and be more time consuming.

The fast optimization derives the Pareto front following the procedure in Fig. 5(b). Assuming there are nine loops for the transmitter and nine loops for the receiver in the lumped-loops model, a total number of 19 simulations are required to derive the permeance matrices and current-to-field matrices, which takes 38 min. After that, the Pareto fronts are derived from calculations with matrices using MATLAB, and only a few seconds are required to calculate each case. Therefore, only 19 simulations are required in the entire procedure of fast optimization, and it is

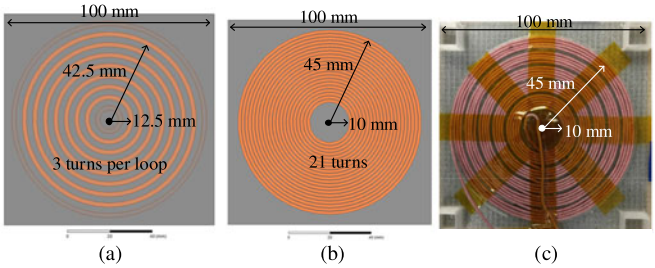

Fig. 14. (a) Selected design of the lumped-loops model along the Pareto front in Fig. 13; (b) coil with real turns translated from the lumped-loops model in (a); (c) fabricated coils according to (b), using litz wire composed of 100 strands with 0.1 mm strand diameter and a 3C96 ferrite plate with dimensions of 100 mm by 100 mm by 5 mm.

TABLE I
INDUCTANCES, WINDING RESISTANCES, AND COIL-TO-COIL EFFICIENCIES FOR COILS IN FIG. 14

Parameters	Matrix Calculation Fig. 14(a)	Simulation Fig. 14(b)	Measurement Fig. 14(c)
L_1, L_2 (μH)	36.9, 36.9	36.8, 36.8	35.4, 36.0
M (μH)	8.6	8.6	8.7
r_1 and r_2 (mΩ), at 100 kHz	100, 100	100, 100	102, 106
Coil-to-coil efficiency	95.7%	95.7%	95.7%

much faster than the conventional method which requires 2070 simulations.

IV. EXPERIMENTAL VERIFICATION

A. Coil-to-Coil Efficiency

One of the optimal designs is selected along the Pareto front in Fig. 13. The lumped-loops model contains nine loops for the transmitter and nine loops for the receiver, as shown in Fig. 14(a). Its permeance matrices are derived from one simulation, and the current-to-field matrices are derived from 18 simulations. Its turns vectors are

$$\vec{N}_{TX} = \begin{bmatrix} 0 & 3 & 3 & 3 & 3 & 3 & 3 & 3 & 0 \end{bmatrix} \quad (32)$$

$$\vec{N}_{RX} = \begin{bmatrix} 0 & 3 & 3 & 3 & 3 & 3 & 3 & 3 & 0 \end{bmatrix}. \quad (33)$$

Litz wire composed of 100 strands with 0.1 mm strand-diameter is used for the winding. The coil with real turns in Fig. 14(b) is derived from the lumped-loops model in Fig. 14(a). There are 21 turns of the winding. The inner radius is 10 mm and the outer radius is 45 mm. Fig. 14(c) is the coil fabricated using the parameters in Fig. 14(b). A 3C96 ferrite plate with dimensions of 100 mm by 100 mm by 5 mm is placed underneath the winding.

Table I shows the inductances and winding resistances of the coils in Fig. 14(a), (b), and (c), which are derived from matrix calculation, finite-element simulation, and measurement, respectively. The matrix calculation and simulation results are almost the same. The maximum difference between calculation and measurement is 4% for inductances and 6% for winding resistances. One reason for the error is the deviation of the turns' radius during the fabrication process.

The coil-to-coil efficiencies in Table I are calculated using (7) with the inductances and winding resistances. All the coils in Fig. 14 achieve 95.7% efficiency for the same specifications in Fig. 4.

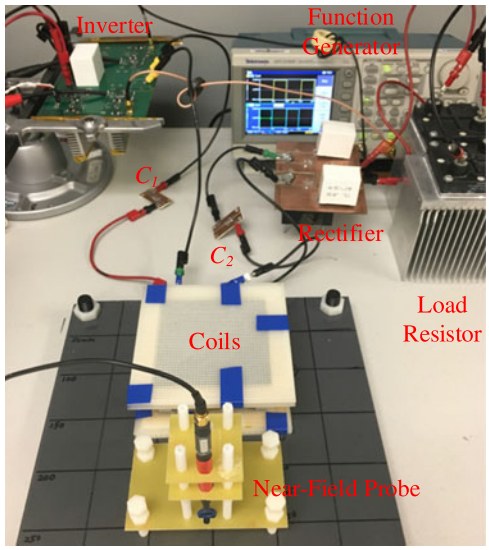

Fig. 15. Hardware setup for field measurement of the coils in Fig. 14(c).

B. Stray Magnetic Field

Fig. 15 shows the hardware setup for field measurement of the coils in Fig. 14(c). Specifications of the experimental measurement are the same as those in Figs. 4 and 13. The power of 100 W was transferred across a 40 mm gap using the circuit topology in Fig. 1(a), with 35 V output voltage and 100 kHz switching frequency. The input dc voltage was adjusted for the desired output power. The measured currents match well with the calculation results using (10) and (11). For each position, the near-field probe Langer EMV LF-R 50 was used to measure magnetic fields $B_X(t)$, $B_Y(t)$, and $B_Z(t)$ in the X, Y, and Z orientations. The quantified magnetic fields were calculated using (15).

With a 40 mm gap between the transmitter and receiver coils, magnetic fields along the *Y*-axis in Fig. 16(a) were calculated, simulated, and measured for the coils in Fig. 14(a), (b), and (c). The quantified magnetic field is shown in Fig. 16(b). The points of field measurement are located along the *Y*-axis, and their distances to the center of the coils range from 75 to 150 mm. The difference between measurement and calculation is less than 12.5%.

Fig. 16(c) and (d) show the time-domain waveforms of stray magnetic fields in the *Y* and *Z* orientations at two positions. One position is 100 mm away from the center, and the other is 150 mm away. The dashed lines are the calculated results of the lumped-loops model in Fig. 14(a), and the solid lines are the measured results of the coils in Fig. 14(c) using the hardware setup in Fig. 15. The measured waveforms are not purely sinusoidal because of the harmonics in the winding currents.

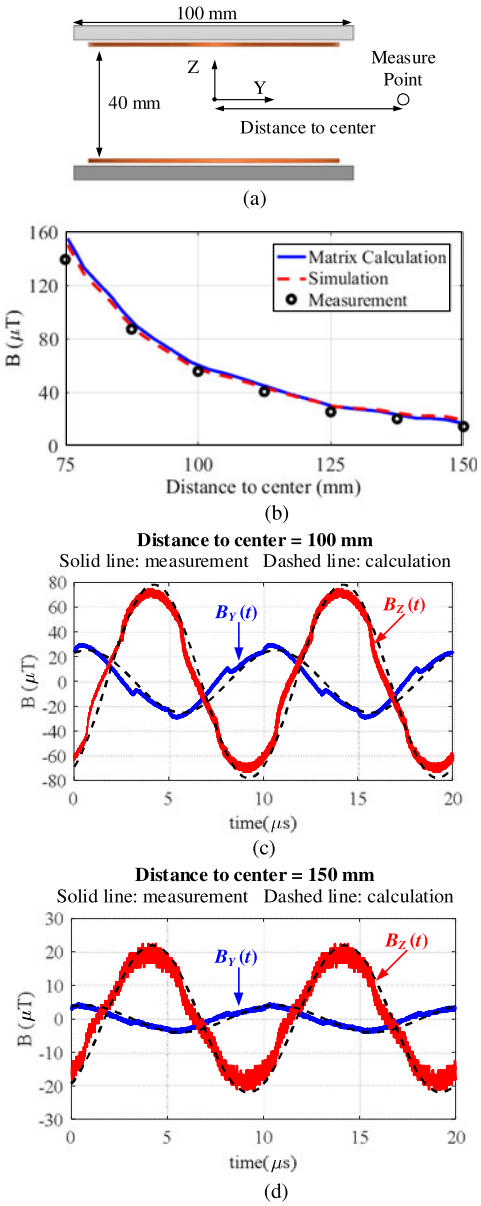

Fig. 16. (a) Side view of the coils and points for field measurement along the *Y*-axis; (b) quantified stray magnetic fields along *Y*-axis, which are calculated, simulated, and measured with the coils in Fig. 14(a), (b), and (c), respectively; (c)–(d) time-domain waveforms of the stray magnetic fields in the *Y* and *Z* orientations at two positions [solid lines: measurement results of the coils in Fig. 14(c); dashed lines: calculation results of the lumped-loops model in Fig. 14(a)].

However, the influence of this nonsinusoidal effect is negligible when quantifying the magnetic fields.

V. Conclusion

The synergetic optimization of IPT coils is discussed in this paper for the coil-to-coil efficiency and stray magnetic field. Pareto front is applied for the optimization. One method to derive the Pareto front is using parametric sweep in finite-element simulation. This method is time consuming especially for 3-D simulation, since two simulations are required for each set of physical parameters. A faster method using lumped-loops model is described in this paper. The coil-to-coil efficiency and stray magnetic field are calculated using permeance matrices, current-to-field matrices, and turns vectors of the lumped-loops model. The sweep of the physical parameters in finite-element simulation is replaced by the sweep of turns vectors in calculation. Only tens of simulations are required during the entire procedure, so this method is much faster than parametric sweep, which requires thousands of simulations. The Pareto front derived from lumped-loops model matches well with that derived from parametric sweep in simulation. Accuracy of the calculation using lumped-loops model is verified using experimental measurement of fabricated coils. The coil-to-coil efficiencies are the same for calculation and measurement, and the difference for stray magnetic field is less than 12.5%.

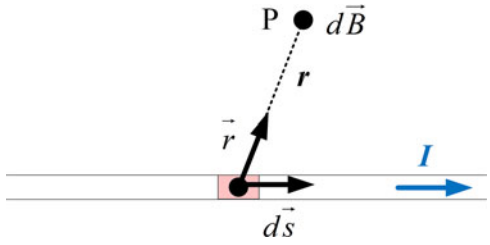

Fig. 17. Magnetic field $d\vec{s}$ at measurement point P generated by the small segment of conductor $d\vec{s}$ with current excitation *I*.

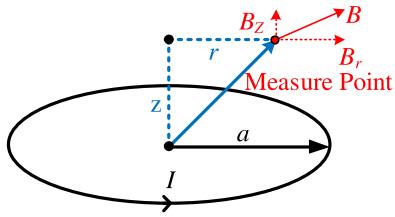

Fig. 18. The example used to calculate magnetic field *B* at the measurement point, which is generated by a circular loop with excitation *I*. Components of *B* include B_r in the radial direction and B_z in the axial direction.

Appendix

The Biot–Savart Law is used to calculate the magnetic field generated by conductors with an air core. The field generated by the small segment of conductor $d\vec{s}$ with length *ds* and excitation current *I* in Fig. 17 is calculated as

$$d\vec{B} = \frac{\mu_0 I}{4\pi} \cdot \frac{d\vec{s} \times \vec{r}}{r^2} \tag{34}$$

where *r* is the distance from the segment to the measure point P; $\vec{r}$ is the unit vector pointing from the segment to P; μ_0 is the permeability of free space.

The magnetic field generated by the circular loop in Fig. 18 is calculated by integrating (34) along the loop. The magnetic fields in the radial and axial directions B_r and B_z at the

measurement point are

$$B_r = \frac{\mu_0 \cdot I \cdot a \cdot z}{4\pi} \int_0^{2\pi} \frac{\sin\varphi}{\left(a^2 + r^2 + z^2 - 2r \cdot a \sin\varphi\right)^{3/2}} d\varphi \tag{35}$$

$$B_z = \frac{\mu_0 \cdot I \cdot a}{4\pi} \int_0^{2\pi} \frac{a - r \cdot \sin\varphi}{\left(a^2 + r^2 + z^2 - 2r \cdot a \cdot \sin\varphi\right)^{3/2}} d\varphi \tag{36}$$

where *I* and *a* are the peak current and radii of the circular loop, respectively; *r* and *z* are the distances in the radial and axial directions between the center of the loop and the measurement point.

Equations (35) and (36) are calculated as

$$B_r = B_0 \frac{\gamma}{\pi\sqrt{Q}} \left[E(k) \frac{1 + \alpha^2 + \beta^2}{Q - 4\alpha} - K(k) \right] \tag{37}$$

$$B_z = B_0 \frac{1}{\pi\sqrt{Q}} \left[E(k) \frac{1 - \alpha^2 - \beta^2}{Q - 4\alpha} + K(k) \right] \tag{38}$$

where functions *K*(*k*) and *E*(*k*) are the complete elliptic integral functions of the first kind and second kind; definitions of B_0, α, β, γ, Q, and *k* are

$$B_0 = (\mu_0 I) / (2a) \tag{39}$$

$$\alpha = r/a \tag{40}$$

$$\beta = z/a \tag{41}$$

$$\gamma = z/r \tag{42}$$

$$Q = \left[(1 + \alpha)^2 + \beta^2 \right] \tag{43}$$

$$k = \sqrt{4\alpha/Q}. \tag{44}$$

REFERENCES

[1] S. Y. R. Hui, W. Zhong, and C. K. Lee, "A critical review of recent progress in Mid-Range wireless power transfer," *IEEE Trans. Power Electron.*, vol. 29, no. 9, pp. 4500–4511, Sep. 2014.

[2] G. A. Covic and J. T. Boys, "Modern trends in inductive power transfer for transportation applications," *IEEE J. Emerg. Sel. Topics Power Electron.*, vol. 1, no. 1, pp. 28–41, Mar. 2013.

[3] S. Li and C. C. Mi, "Wireless power transfer for electric vehicle applications," *IEEE J. Emerg. Sel. Topics Power Electron.*, vol. 3, no. 1, pp. 4–17, Mar. 2015.

[4] R. Bosshard and J. W. Kolar, "Inductive power transfer for electric vehicle charging: Technical challenges and tradeoffs," *IEEE Power Electron. Mag.*, vol. 3, no. 3, pp. 22–30, Sep. 2016.

[5] C.-S. Wang, O. H. Stielau, and G. A. Covic, "Design considerations for a contactless electric vehicle battery charger," *IEEE Trans. Ind. Electron.*, vol. 52, no. 5, pp. 1308–1314, Oct. 2005.

[6] J. L. Villa, J. Sallan, J. F. Sanz Osorio, and A. Llombart, "High-misalignment tolerant compensation topology for ICPT systems," *IEEE Trans. Ind. Electron.*, vol. 59, no. 2, pp. 945–951, Feb. 2012.

[7] N. A. Keeling, G. A. Covic, and J. T. Boys, "A unity-power-factor IPT pickup for high-power applications," *IEEE Trans. Ind. Electron.*, vol. 57, no. 2, pp. 744–751, Feb. 2010.

[8] B. Esteban, M. Sid-Ahmed, and N. C. Kar, "A comparative study of power supply architectures in wireless EV charging systems," *IEEE Trans. Power Electron.*, vol. 30, no. 11, pp. 6408–6422, Nov. 2015.

[9] L. Kibok, Z. Pantic, and S. M. Lukic, "Reflexive field containment in dynamic inductive power transfer systems," *IEEE Trans. Power Electron.*, vol. 29, no. 9, pp. 4592–4602, Sep. 2014.

[10] J. M. Miller, P. T. Jones, J. M. Li, and O. C. Onar, "ORNL experience and challenges facing dynamic wireless power charging of EV's," *IEEE Circuits Syst. Mag.*, vol. 15, no. 2, pp. 40–53, Secondquarter 2015.

[11] E. Waffenschmidt and T. Staring, "Limitation of inductive power transfer for consumer applications," in *Proc. Eur. Conf. Power Electron. Appl.*, 2009, pp. 1–10.

[12] R. Bosshard, J. W. Kolar, J. Muhlethaler, I. Stevanovic, B. Wunsch, and F. Canales, "Modeling and η-α-Pareto optimization of inductive power transfer coils for electric vehicles," *IEEE J. Emerg. Sel. Topics Power Electron.*, vol. 3, no. 1, pp. 50–64, Mar. 2015.

[13] T. Diekhans and R. W. De Doncker, "A dual-side controlled inductive power transfer system optimized for large coupling factor variations and partial load," *IEEE Trans. Power Electron.*, vol. 30, no. 11, pp. 6320–6328, Nov. 2015.

[14] G. Buja, M. Bertoluzzo, and K. N. Mude, "Design and experimentation of WPT charger for electric city car," *IEEE Trans. Ind. Electron.*, vol. 62, no. 12, pp. 7436–7447, Dec. 2015.

[15] R. Bosshard, J. W. Kolar, and B. Wunsch, "Accurate finite-element modeling and experimental verification of inductive power transfer coil design," in *Proc. IEEE 29th Annu. IEEE Appl. Power Electron. Conf. Expo.*, 2014, pp. 1648–1653.

[16] O. H. Stielau and G. A. Covic, "Design of loosely coupled inductive power transfer systems," in *Proc. Int. Conf. Power Syst. Technol.*, 2000, vol. 1, pp. 85–90.

[17] C. Rui *et al.*, "Analysis and parameters optimization of a contactless IPT system for EV charger," in *Proc. 29th Annu. IEEE Appl. Power Electron. Conf. Expo.*, 2014, pp. 1654–1661.

[18] M. Lu and K. D. T. Ngo, "Sequential design for coils in series-series inductive power transfer using normalized parameters," in *Proc. 2016 IEEE PELS Workshop Emerg. Technol.: Wireless Power*, Knoxville, TN, USA, 2016, pp. 1–6.

[19] J. L. Volakis, *Antenna Engineering Handbook*, 4th ed. New York, NY, USA: McGraw-Hill, 2007.

[20] "ICNIRP guidelines for limiting exposure to time-varying electric, magnetic and electromagnetic fields (1 Hz to 100 kHz)," *Health Phys.*, vol. 99, pp. 818–836, 2010.

[21] M. Lu and K. D. T. Ngo, "Pareto fronts for coils' efficiency versus stray magnetic field in inductive power transfer," in *Proc. 2016 IEEE PELS Workshop Emerg. Technol.: Wireless Power*, Knoxville, TN, USA, 2016, pp. 1–5.

[22] H. Kim, C. Song, J. Kim, and D. Jung, "Design of magnetic shielding for reduction of magnetic near field from wireless power transfer system for electric vehicle," in *Proc. 2014 Int. Symp. Electromagn. Compat.*, Gothenburg, Sweden, 2014, pp. 53–58.

[23] J. W. Kolar, J. Biela, and J. Minibock, "Exploring the pareto front of multi-objective single-phase PFC rectifier design optimization −99.2% efficiency vs. 7 kW/din3 power density," in *Proc. 2009 IEEE 6th Int. Power Electron. Motion Control Conf.*, Wuhan, China, 2009, pp. 1–21.

[24] J. A. Ferreira, "Improved analytical modeling of conductive losses in magnetic components," *IEEE Trans. Power Electron.*, vol. 9, no. 1, pp. 127–131, Jan. 1994.

[25] C. R. Sullivan, "Computationally efficient winding loss calculation with multiple windings, arbitrary waveforms, and two-dimensional or three-dimensional field geometry," *IEEE Trans. Power Electron.*, vol. 16, no. 1, pp. 142–150, Jan. 2001.

[26] I. Lope, J. Acero, and C. Carretero, "Analysis and optimization of the efficiency of induction heating applications with Litz-Wire planar and solenoidal coils," *IEEE Trans. Power Electron.*, vol. 31, no. 7, pp. 5089–5101, Jul. 2016.

[27] J. Mühlethaler, "Modeling and multi-objective optimization of inductive power components," Ph.D. dissertation, Swiss Federal Inst. Technol. Zurich, ETHZ, Zürich, Switzerland, 2012.

[28] M. Lu and K. D. T. Ngo, "Comparison of passive shields for coils in inductive power transfer," in *Proc. 2017 IEEE Appl. Power Electron. Conf. Expo.*, Tampa, FL, USA, 2017, pp. 1419–1424.

[29] M. Lu and K. D. T. Ngo, "Synergetic optimization of efficiency and stray magnetic field for planar coils in inductive power transfer using matrix calculation," in *Proc. 32nd Annu. IEEE Appl. Power Electron. Conf. Expo.*, Tampa, FL, USA, Mar. 2017, pp. 3654–3660.

[30] Ansys. Mar. 2012 User's Guide-Maxwell 3-D, Rev 6.0. [Online]. Available: http://ansoft-maxwell.narod.ru/english.html

[31] E. Waffenschmidt, "Homogeneous magnetic coupling for free positioning in an inductive wireless power system," *IEEE J. Emerg. Sel. Topics Power Electron.*, vol. 3, no. 1, pp. 226–233, Mar. 2015.
[32] A. V. den Bossche and V. C. Valchev, *Inductors and Transformers for Power Electronics*. Boca Raton, FL, US: CRC Press, 2005.
[33] W. A. Roshen and D. E. Turcotte, "Planar inductors on magnetic substrates," *IEEE Trans. Magn.*, vol. 24, no. 6, pp. 3213–3216, Nov. 1988.
[34] J. Muhlethaler, M. Schweizer, R. Blattmann, J. W. Kolar, and A. Ecklebe, "Optimal design of LCL harmonic filters for three-phase PFC rectifiers," *IEEE Trans. Power Electron.*, vol. 28, no. 7, pp. 3114–3125, Jul. 2013.
[35] M. Curti, J. J. H. Paulides, and E. A. Lomonova, "An overview of analytical methods for magnetic field computation," in *Proc. 2015 10th Int. Conf. Ecological Veh. Renewable Energies*, 2015, pp. 1–7.
[36] S. Ramo, J. R. Whinnery, and T. Van Dum, *Fields and Waves in Communication Electronics*. New York, NY, USA: Wiley, 1965.

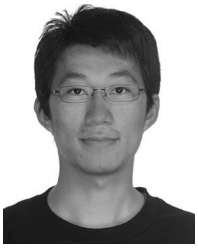

Ming Lu (S'16) received the B.S. and M.S. degrees from Shanghai Jiao Tong University, Shanghai, China, in 2008 and 2012, respectively, both in electrical engineering. He is currently working toward the Ph.D. degree in electrical engineering at the Center for Power Electronics Systems, Virginia Tech, Blacksburg, VA, USA.

His current research interests include wireless power transfer for electric vehicles and wide bandgap power semiconductor devices.

Khai D. T. Ngo (S'82–M'84–SM'02–F'15) received the B.S. degree from California State Polytechnic University, Pomona, Pomona, CA, USA, in 1979, and the M.S. and Ph.D. degrees from the California Institute of Technology, Pasadena, Pasadena, CA, USA, in 1980 and 1984, respectively, all in electrical and electronics engineering.

He is currently a Professor of electrical and computer engineering at Virginia Tech, Blacksburg, VA, USA. He was a member of Technical Staff at General Electric Corporate Research and Development Center, Schenectady, NY, USA, from 1984 to 1988. Between 1988 and 2006, he was with the University of Florida, Gainesville, FL, USA. At Virginia Tech, he pursues technologies for integration and packaging of power passive and active components to realize building blocks for power electronic systems. These technologies lead to power conversion systems with higher efficiency and higher power density. He also focuses on topologies, control, emission, and integration issues for RF power converters. Other research interests include magnetic materials and components, energy reclamation, and power integrated circuits.